Solid energy calibration standards for P K-edge XANES: electronic structure analysis of PPh$_4$Br

Anastasia V. Blake,[a] Haochuan Wei,[b] Courtney M. Donahue,[a] Kyounghoon Lee,[a] Jason M. Keith[b]* and Scott R. Daly[a]*

[a]The University of Iowa, Department of Chemistry, E331 Chemistry Building, Iowa City, IA 52242, USA, and [b]Department of Chemistry, Colgate University, 13 Oak Drive, Hamilton, NY 13346, USA. *Correspondence e-mail: jkeith@colgate.edu, scott-daly@uiowa.edu

P K-edge X-ray absorption near-edge structure (XANES) spectroscopy is a powerful method for analyzing the electronic structure of organic and inorganic phosphorus compounds. Like all XANES experiments, P K-edge XANES requires well defined and readily accessible calibration standards for energy referencing so that spectra collected at different beamlines or under different conditions can be compared. This is especially true for ligand K-edge X-ray absorption spectroscopy, which has well established energy calibration standards for Cl (Cs$_2$CuCl$_4$) and S (Na$_2$S$_2$O$_3$·5H$_2$O), but not neighboring P. This paper presents a review of common P K-edge XANES energy calibration standards and analysis of PPh$_4$Br as a potential alternative. The P K-edge XANES region of commercially available PPh$_4$Br revealed a single, highly resolved pre-edge feature with a maximum at 2146.96 eV. PPh$_4$Br also showed no evidence of photodecomposition when repeatedly scanned over the course of several days. In contrast, we found that PPh$_3$ rapidly decomposes under identical conditions. Density functional theory calculations performed on PPh$_3$ and PPh$_4^+$ revealed large differences in the molecular orbital energies that were ascribed to differences in the phosphorus oxidation state (III *versus* V) and molecular charge (neutral *versus* +1). Time-dependent density functional theory calculations corroborated the experimental data and allowed the spectral features to be assigned. The first pre-edge feature in the P K-edge XANES spectrum of PPh$_4$Br was assigned to P $1s \rightarrow$ P-C π* transitions, whereas those at higher energy were P $1s \rightarrow$ P-C σ*. Overall, the analysis suggests that PPh$_4$Br is an excellent alternative to other solid energy calibration standards commonly used in P K-edge XANES experiments.

1. Introduction

P K-edge X-ray absorption near-edge structure (XANES) spectroscopy is a powerful method for analyzing organic and inorganic compounds containing phosphorus. Electronic transitions at the P K-edge occur in the 'tender' X-ray region (P $1s$ binding energy = 2145.5 eV), and the resulting spectra have sufficient resolution for quantitative electronic structure comparisons and utility in diverse applications (Northrup *et al.*, 2016). For example, P K-edge XANES has been used to identify phosphorus-containing chemicals in soil and other complex mixtures, especially those encountered in agricultural, environmental and tribological-related samples (Ingall *et al.*, 2011; Yoshida *et al.*, 2016; Morel *et al.*, 2015; Tan *et al.*, 2014; Kasrai *et al.*, 1999; Zhang *et al.*, 2005; Pereira *et al.*, 2006, 2007; Sharma *et al.*, 2016). It has also been used to quantify relative differences in covalent metal–phosphorus bonding and electronic structure in coordination compounds containing phosphorus ligands (Adhikari *et al.*, 2008; Harkins *et al.*, 2008; Mankad *et al.*, 2009; Mossin *et al.*, 2012; Shearer *et*

2146.96 2149.85   PPh$_4$Br
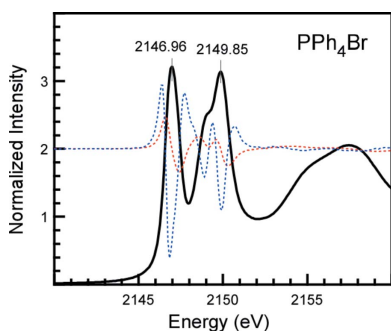
al., 2012; Soma *et al.*, 2016; Hu *et al.*, 2015; Donahue *et al.*, 2015; Lee *et al.*, 2016). This latter type of metal–ligand bonding analysis is more generally referred to as ligand *K*-edge X-ray absorption spectroscopy (XAS) (Solomon *et al.*, 2005; Glaser *et al.*, 2000; Queen *et al.*, 2013).

As with all XANES measurements, ligand *K*-edge XAS requires a convenient and well defined energy calibration standard so that accurate comparisons can be made between different data sets collected at different synchrotron facilities. Photodecomposition-resistant energy standards with intense, highly resolved pre-edge features have long been established for referencing ligand *K*-edge XAS data with the third row elements chlorine (Cs_2CuCl_4) and sulfur ($Na_2S_2O_3 \cdot 5H_2O$) (Solomon *et al.*, 2005). At the beginning of our electronic structure investigations of metal-phosphine complexes (Donahue *et al.*, 2015), we sought a well defined solid energy standard for *K*-edge XANES measurements with phosphorus (which neighbors sulfur and chlorine) and found, unexpectedly, that a single reference had yet to be established for ligand *K*-edge XAS studies. Numerous phosphorus compounds have been used as energy standards, and much of this data comes from researchers using P *K*-edge XANES in applications other than ligand *K*-edge XAS.

Here we provide a brief, but critical, review of commonly used P *K*-edge energy standards, and report the P *K*-edge XANES spectrum and density functional theory (DFT) calculations of PPh_4Br. This compound has worked extremely well as a P *K*-edge energy calibration standard for ligand *K*-edge XAS studies (Lee *et al.*, 2016), and offers several advantages over other calibration standards.

2. Experimental

$Na_4P_2O_7$, $OPPh_3$ and PPh_4Br were purchased from commercial vendors in their highest available purity and used as received. PPh_3 was recrystallized from distilled EtOH and analyzed by ^{31}P NMR spectroscopy before use to ensure that no $OPPh_3$ impurity was present.

2.1. XAS data collection and analysis

P *K*-edge XAS data were collected at beamline 14-3 at the Stanford Synchrotron Radiation Lightsource under dedicated operating conditions of 3.0 GeV and 500 mA using beamline optics and equipment described previously (Lee *et al.*, 2016). Beamline 14-3 has a bending-magnet source and a water-cooled double Si(111) crystal monochromator. The sample chamber was maintained under a He atmosphere and sample fluorescence was measured using a PIPS or Vortex detector with the sample placed at a 45° angle with respect to the incident beam. The beam spot size was $\leq 3\ mm^2$ and the flux was *ca.* 2×10^{10} photons s^{-1}. No filters were used. Samples were finely ground using a Wig-L-Bug grinder for two minutes and thinly painted on Kapton tape with a size 4 Blick Scholastic Wonder White Flat synthetic brush (or equivalent) to minimize self-absorption effects. This was confirmed by analyzing progressively thicker layers to identify

the onset of observable self-absorption effects in the spectra. P *K*-edge XAS data were collected over three regions with 1.0 eV steps and 1.0 s dwell times between 2106 and 2136 eV (pre-edge), 0.08 eV steps and 1–2 s dwell times between 2136 and 2165 eV (edge), and 1.5 eV steps and 1 s dwell times between 2165 and 2380 eV (post-edge). Data were collected in triplicate scans over several experimental runs. P *K*-edge XAS data were calibrated to the white line of $Na_4P_2O_7$ at 2152.40 eV (Fig. 1). Calibration scans were collected before and after each triplicate data set.

Calibrations, background subtractions, normalizations and averaging were performed using the *Athena* program in the *IFFEFIT* XAS software package (Ravel & Newville, 2005). All scans were ratioed against the incident radiation (I0), which was measured using an ionization chamber located prior to the sample chamber. Subsequent pre-edge and post-edge
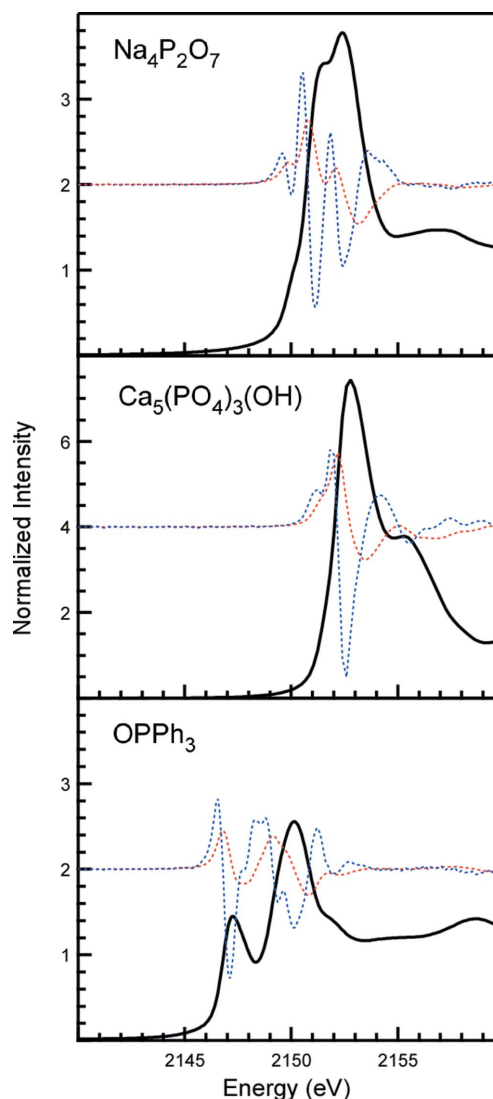
fits for background subtractions and normalizations were performed as previously described (Donahue *et al.*, 2015; Lee *et al.*, 2016). The background was removed from each spectrum by fitting a first-order polynomial to the pre-edge region. The data were normalized by fitting the post-edge region with a first- or second-order polynomial. The step function intensity for data normalizations was set to 1.0 at 2165 eV. Curve fits were performed using *IGOR Pro* 6.3 using a modified version of *EDGEFIT*, as described previously (Donahue *et al.*, 2015; Lee *et al.*, 2016).

2.2. DFT and TDDFT calculations

DFT calculations were performed as described previously using the *Gaussian09* computational chemistry suite (Frisch *et al.*, 2009; Lee *et al.*, 2016). To summarize, PPh_3 and PPh_4^+ were evaluated at the dispersion-corrected hybrid density functional theory level known as B3LYP-d3 with the three-parameter exchange functional of Becke (Becke, 1993), the correlation functional of Lee, Yang and Parr (Lee *et al.*, 1988), and the addition of empirical dispersion with Grimme's D3 dispersion corrections (Grimme *et al.*, 2010). All atoms were modeled with the split-valence double-ζ plus polarization basis set 6-31G(d,p) (Hehre *et al.*, 1972; Hariharan & Pople, 1973), and both structures were fully optimized in the gas phase. Frequency calculations were performed to ensure the absence of any imaginary vibrational modes. Wavefunction stability calculations were performed on all species to ensure that the resulting determinant was in fact a local minimum (Bauernschmitt & Ahlrichs, 1996). Time-dependent density functional theory (TDDFT) calculations were conducted to approximate excitation energies and amplitudes (oscillator strengths) for specific excited states, and to simulate the P K-edge XAS spectra. Energy shifts of +50.1 (PPh_3) and +49.6 eV (PPh_4^+) were applied to the simulated transitions and TDDFT spectra to align them with the experimental data. As described previously, this difference in absolute energy arises due to the nonlocal nature of the calculated core hole, the inability to model the relaxation of the core hole, and inaccuracies of the functional. As shown here, once the error in absolute energy has been accounted for by applying a uniform energy shift, the calculations reproduce experimental ligand K-edge XAS data with very high accuracy for a wide-variety of complexes, including those containing transition metals, lanthanides and actinides (Kozimor *et al.*, 2008, 2009; Daly *et al.*, 2012; Minasian *et al.*, 2012, 2014; Spencer *et al.*, 2013; Löble *et al.*, 2015; Donahue *et al.*, 2014, 2015; Olson *et al.*, 2014; Lee *et al.*, 2016).

3. Results and discussion

3.1. Review of common P K-edge XANES energy calibration standards

Numerous compounds have been used for P K-edge XANES energy referencing including $Na_4P_2O_7$ (sodium pyrophosphate) (Blanchard *et al.*, 2008; Grosvenor *et al.*, 2008; Kruse & Leinweber, 2008; Kruse *et al.*, 2010), red phosphorus (Rafiuddin *et al.*, 2014; Prietzel *et al.*, 2016, 2013; Rafiuddin &

Grosvenor, 2016), $AlPO_4 \cdot (H_2O)_n$ (aluminium phosphate; $n = 0$, 1.5 or 2) (Liu *et al.*, 2015, 2013; Kraal *et al.*, 2015; Eveborn *et al.*, 2009; Baumann *et al.*, 2017; Huang & Tang, 2016), $Ca_5(PO_4)_3(OH)$ (hydroxyapatite) (Takamoto & Hashimoto, 2014; Hashimoto *et al.*, 2014), $Zn_3(PO_4)_2$ (Kasrai *et al.*, 1999; Sharma *et al.*, 2016) and $OPPh_3$ (triphenylphosphine oxide) (Adhikari *et al.*, 2008; Harkins *et al.*, 2008; Mankad *et al.*, 2009; Mossin *et al.*, 2012; Shearer *et al.*, 2012; Soma *et al.*, 2016). At the beginning of our P K-edge XAS studies, anhydrous $Na_4P_2O_7$ was selected because it was readily available and had a reference value reported to 0.01 eV precision. The most intense peak (white line) located at 2152.40 eV in the P K-edge XANES spectrum is used for energy referencing (Küper *et al.*, 1994; Engemann *et al.*, 1999). Unfortunately, we discovered that the white line was not well resolved from a lower-energy feature with similar intensity (Fig. 1) and often required longer calibration dwell times to ensure sufficient signal-to-noise for accurate energy referencing *via* analysis of the first derivative trace. Our studies also prompted questions as to how the position of the features changes in response to absorption of water. $Na_4P_2O_7$ is hygroscopic and can absorb up to as many as ten H_2O molecules when exposed to ambient humidity (it is available commercially as an anhydrous powder or decahydrate). It is not clear if variations in $Na_4P_2O_7$ hydration alter the energy and intensities of its P K-edge XANES features, but related hydrogen-bonding interactions are known to cause changes in XANES peak energies and intensities in other compounds (Dey *et al.*, 2005).

We next considered $Ca_5(PO_4)_3(OH)$ (hydroxyapatite) and red phosphorus. Red phosphorus was quickly ruled out because of its reactivity; it slowly oxidizes in air, which has been monitored by *in situ* P K-edge XANES measurements as a function of time and temperature (Küper *et al.*, 1994). In contrast, $Ca_5(PO_4)_3(OH)$ is a highly inert bioceramic found in bones and teeth. It has been studied extensively using P K-edge XANES and has an intense white line ideal for energy referencing. However, the analysis of 17 reported spectra by Oxmann showed subtle variations in the white line energy depending on the $Ca_5(PO_4)_3(OH)$ preparation method and commercial vendor (Oxmann, 2014). It is well known that $Ca_5(PO_4)_3(OH)$ morphology and Ca/P stoichiometry is sensitive to the preparation method used (Ferraz *et al.*, 2004; Raynaud *et al.*, 2002), which is likely to account for the observed spectral differences (Nakahira *et al.*, 2011). It is unclear from Oxmann's plots of $Ca_5(PO_4)_3(OH)$ whether the batch-to-batch differences are severe enough to suggest precluding its use as an energy standard, but these differences, combined with the lack of post-synthetic methods to purify this high-melting ceramic, made it appear less desirable. Similar assessments were made for $AlPO_4 \cdot (H_2O)_n$ and other water-insoluble phosphates and high-melting solids.

We next turned our attention to molecular phosphorus compounds. Triphenylphosphine oxide ($OPPh_3$) has been used for ligand K-edge XAS measurements (Adhikari *et al.*, 2008; Harkins *et al.*, 2008; Mankad *et al.*, 2009; Mossin *et al.*, 2012; Shearer *et al.*, 2012; Soma *et al.*, 2016). $OPPh_3$ has a resolved pre-edge feature and is commercially available (Fig. 1). Unlike

$Na_4P_2O_7$, $OPPh_3$ is hydrophobic with low solubility in water, suggesting that peak positions are less susceptible to hydration effects. While $OPPh_3$ has desirable attributes for a P K-edge XANES energy standard, there are some discrepancies in its reported calibration energy. The first pre-edge maximum has been reported at 2147.3 eV (Küper *et al.*, 1994; Engemann *et al.*, 1999), 2147.5 eV (Adhikari *et al.*, 2008; Harkins *et al.*, 2008; Mankad *et al.*, 2009; Mossin *et al.*, 2012; Shearer *et al.*, 2012) and 2145.7 eV (Soma *et al.*, 2016). However, the latter two energy values were probably annotated incorrectly because they reference the reported value of 2147.3 eV from Hormes and co-workers (Küper *et al.*, 1994; Engemann *et al.*, 1999). To investigate these discrepancies, we collected the P K-edge XANES spectrum of $OPPh_3$. The first peak in $OPPh_3$ was observed at 2147.3 eV when referenced to $Na_4P_2O_7$, matching the value reported previously by Hormes and co-workers.

The use of three different reference values for $OPPh_3$ is not a significant concern as long as people are aware they exist and take them into account when referencing their data to other data sets. However, this is likely to be overlooked. Knowing that future P K-edge XANES users will continue to propagate multiple calibration values for $OPPh_3$, it was important to highlight the differences and describe a potential alternative with a single-reference value for future P K-edge XAS studies.

3.2. Investigation of PPh_3 and PPh_4Br

Our search for an alternative P K-edge XANES standard focused on compounds that could meet the following criteria: (1) have a well resolved pre-edge feature for precise energy calibration, (2) be hydrophobic and resistant to hydrogen-bonding interactions that could perturb the electronic structure of phosphorus, (3) be air-stable, (4) be resistant to photodecomposition, and (5) be commercially available. The first candidate was PPh_3, a commercially available phosphine reported to have a well defined pre-edge feature at 2145.4 eV (Engemann *et al.*, 1999). However, it was soon discovered that PPh_3 undergoes photodecomposition at beamline 14-3 at the Stanford Synchrotron Radiation Lightsource (Fig. 2). The pre-edge peak was observed at 2145.3 eV and decreased as a function of time, and a feature assigned to $OPPh_3$ grew in at
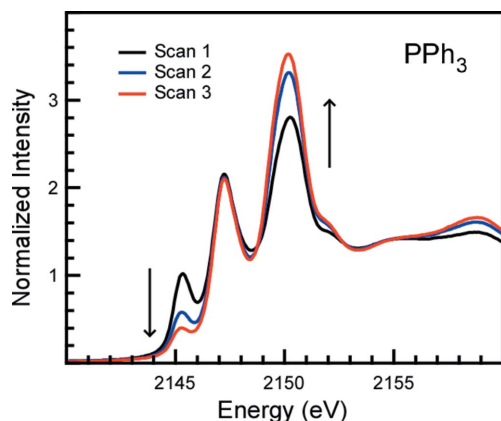

Figure 2
P K-edge XANES spectra of PPh_3 collected at beamline 14-3 at SSRL.

2150.1 eV. This latter peak was not present in P K-edge XANES spectra reported previously for PPh_3 (Engemann *et al.*, 1999; Mankad *et al.*, 2009), indicating that our PPh_3 had already oxidized to some extent before the first scan was collected. The peak at *ca.* 2147.3 eV is present in the spectra of both PPh_3 and $OPPh_3$, and therefore does not change significantly in intensity as PPh_3 oxidation occurs. The presence of other $OPPh_3$ transitions accounts for the slight discrepancy in our measured PPh_3 pre-edge feature at 2145.3 eV compared with the value reported previously for oxide-free PPh_3 at 2145.4 eV (Engemann *et al.*, 1999).

The lack of decomposition in earlier P K-edge XAS data sets collected for PPh_3 can likely be ascribed to the spectra collection using unfocused beams (Mankad *et al.*, 2009; Engemann *et al.*, 1999). In contrast, our data were collected using a focused beam at a beamline typically configured for imaging work. While the observed photodecomposition indicated PPh_3 was not a suitable calibration standard, the experiments revealed that beamline 14-3 at SSRL would provide an excellent proving ground to test the photostability of other potential P K-edge XANES standards.

We next investigated PPh_4Br. PPh_4^+ is a common non-coordinating cation used in coordination chemistry to offset the charge of complex ions (Daly *et al.*, 2012; Minasian *et al.*, 2012; Donahue *et al.*, 2014; Olson *et al.*, 2014), and is commercially available as its chloride and bromide salt. We reasoned that PPh_4^+ should be more stable than PPh_3 with respect to photodecomposition; PPh_4^+ is a fully oxidized P(V) complex like $OPPh_3$, which is corroborated by our P K-edge XANES data (see below). We postulated that the higher symmetry of PPh_4^+ *versus* $OPPh_3$ (and corresponding differences in selection rules) would lead to a more resolved pre-edge feature in the P K-edge XANES spectrum, thereby making it more ideal for energy referencing. If one considers only the carbon and oxygen atoms attached to phosphorus, the point group symmetry of PPh_4^+ is T_d whereas for $OPPh_3$ it is C_{3V}. As discussed below, the actual point group symmetries are slightly lower when the orientation of the phenyl groups are taken into consideration.

The P K-edge XAS spectrum of PPh_4Br is provided in Fig. 3. Unlike PPh_3, no decomposition was observed over repeated scans performed intermittently on the same sample over one week (we used the same sample for calibration scans over an entire week of data collection). Three prominent features were observed prior to the higher energy shape resonances starting at 2153 eV. The first derivative trace revealed two maxima (*i.e.* where the first derivative trace crosses 0) at 2146.96 and 2149.85 eV. The second derivative trace was used to assign the energy of the shoulder located next to the peak at 2149.85 eV and identify underlying features contributing to the observed peaks. Three minima were observed at 2146.82, 2148.90 and 2149.90 eV corresponding to the three most prominent XANES features. In addition, peak shouldering was observed in the second derivative trace at approximately 2147.2 and 2148.1 eV (Fig. 4). No lower energy pre-edge features were observed in the range known for P(III) complexes such as PPh_3 (2145.4 eV; Fig. 2) or PEt_3 (2145.8 eV)
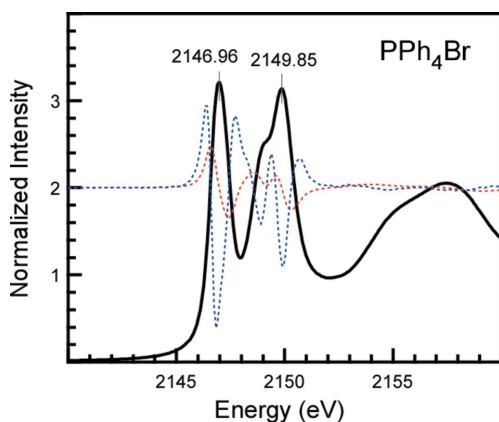
Figure 3
P K-edge XANES spectrum of PPh₄Br. First and second derivative traces, depicted with red and blue dashed lines, respectively, are offset on the y-axis by +2 intensity units.

(Engemann *et al.*, 1999), consistent with the assignment of PPh₄⁺ as a P(V) complex. The peak positions fall within the range of those described for OPPh₃ and other P(V) complexes with phenyl substituents (SPPh₃ and SePPh₃) (Engemann *et al.*, 1999).

Our P K-edge peak positions for PPh₄Br are reported with 0.01 eV precision based on the following justification. First, all of our spectra are referenced to the white line for $Na_4P_2O_7$ at 2152.40 ± 0.05 eV (Küper *et al.*, 1994; Engemann *et al.*, 1999). This value was determined by Hormes and co-workers using a double InSb(111) crystal monochromator calibrated to the Ar K-edge of argon gas at 3203.54 eV (Küper *et al.*, 1994). Second, spectra from each run were obtained by averaging no less than three scans individually calibrated to $Na_4P_2O_7$. Positions were then obtained from the first derivative trace of the merged scan, so peak positions were not limited by the 0.08 eV step size used over the edge in our experiments. Finally, averaged scans from multiple runs were used to establish a standard deviation in the peak position, which was ± 0.02 eV. This measured repeatability is better than the ~ 0.1 eV energy reproducibility used to establish the Cs_2CuCl_4
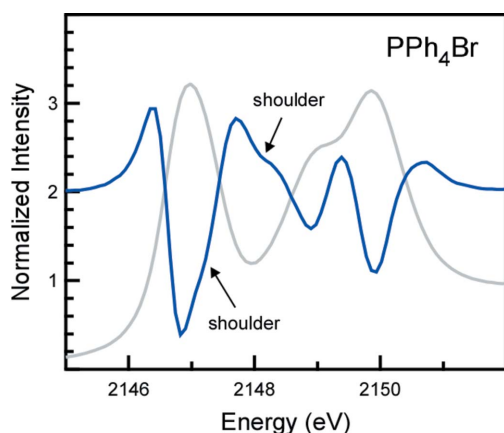

Figure 4
Enlarged P K-edge XANES spectrum (grey) and second derivative trace (blue) of PPh₄Br. The second derivative trace is offset on the y-axis by +2 intensity units and scaled for comparison with the XANES trace.

and $Na_2SO_3 \cdot 5H_2O$ pre-edge peak positions at 2820.20 eV and 2472.02 eV, respectively, for use as Cl and S K-edge XAS energy calibration standards (Solomon *et al.*, 2005).

It is important to note that peak positions can change slightly depending on the resolution of the beamline used. While a theoretical resolution can be calculated based on the monochromator crystals and energy of the element edge, the actual resolution of the beamline depends on the experimental setup and can be difficult to measure in a reliable way. To address this issue, we have uploaded our normalized P K-edge XAS data of PPh₄Br in the supporting information. We also curve-fit our spectra to obtain the full width at half-maximum (FWHM) of our first pre-edge feature. As described by Solomon *et al.* (2005) for ligand K-edge XAS data, the spectra were modeled with pseudo-Voigt functions containing 1:1 mixtures of Gaussian and Lorentzian lineshapes. The step function was modeled with 1:1 ratio of arctangent and error function contributions. Curve fits of nine P K-edge XANES spectra of PPh₄Br gave an average FWHM of 1.02 ± 0.03 eV for the first pre-edge peak.

3.3. DFT and TDDFT calculations

DFT and TDDFT calculations were performed on PPh₄⁺ to assign features in the P K-edge XANES spectrum. Calculations were also performed on the aforementioned PPh₃ to compare how changes in oxidation state and symmetry affected the electronic structure. Optimized gas-phase structures of PPh₃ and PPh₄⁺ are provided in Fig. 5 and a truncated molecular orbital (MO) diagram is provided in Fig. 6. C_3 and D_{2d} point group symmetries were assigned to the calculated structures of PPh₃ and PPh₄⁺, respectively, which take into account the phenyl group orientations. Mulliken symbols were assigned by analyzing the symmetry of the Kohn–Sham orbitals, as shown in Fig. 6 for the highest occupied molecular orbitals (HOMO) and lowest unoccupied molecular orbitals (LUMO).

The calculated MOs for PPh₄⁺ all decrease in energy relative to PPh₃ as a result of the change in P oxidation state and molecular charge (+1 and 0). The HOMO for PPh₃ (1a) is
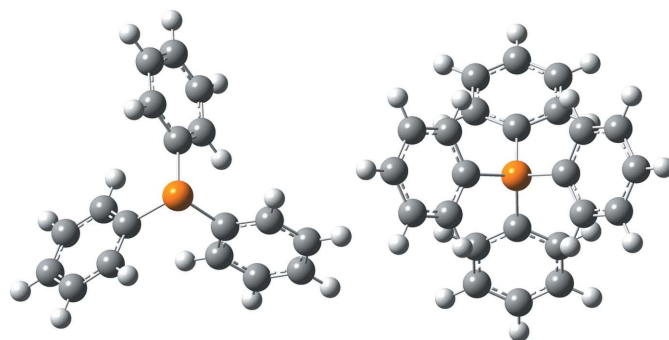

Figure 5
Calculated structures of PPh₃ (left) and PPh₄⁺ (right). P—C bond distances: 1.851–1.852 Å (PPh₃) and 1.812 Å (PPh₄⁺); C—P—C bond angles = 101.7° (PPh₃) and 110.3° (PPh₄⁺). The bond distances and angles are nearly identical to those obtained experimentally by single-crystal XRD (Alcock *et al.*, 1985; Dunne & Orpen, 1991).
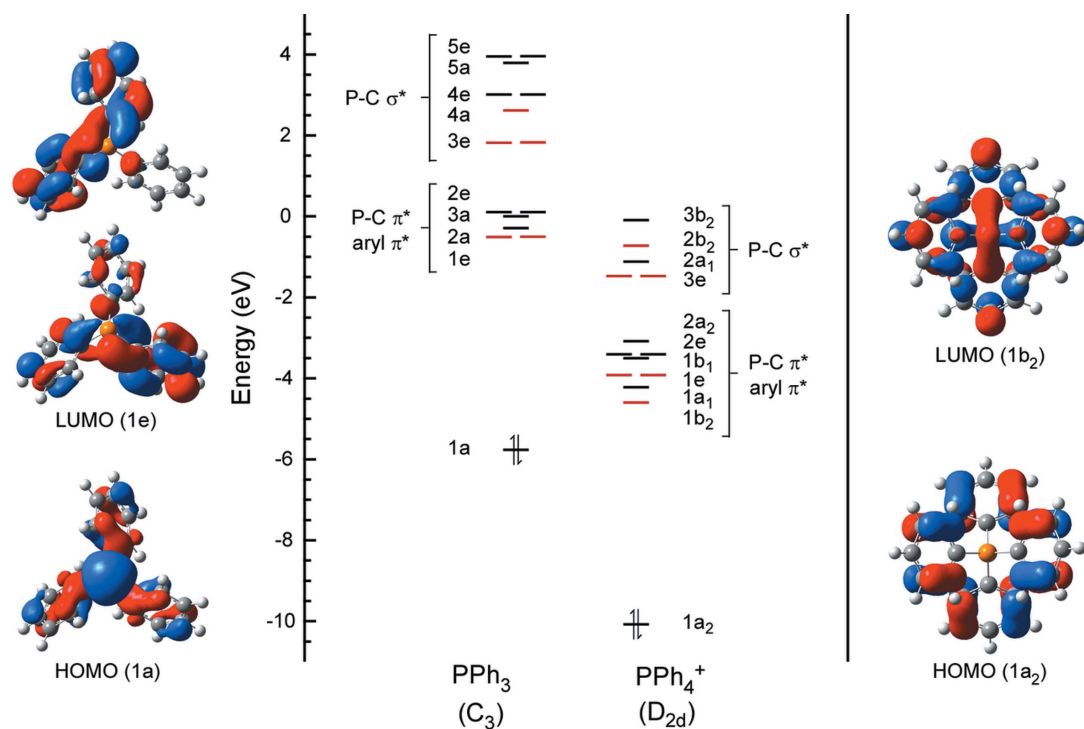
Figure 6
Molecular orbital diagram of PPh$_3$ and PPh$_4^+$ from DFT calculations. Kohn–Sham orbitals of the highest occupied and lowest unoccupied molecular orbitals are shown on the left (PPh$_3$) and right (PPh$_4^+$). Unoccupied MOs depicted in red are those involved in the calculated P K-edge XAS transitions (TDDFT) in Fig. 7.

effectively the P lone pair with some phenyl mixing (33.7% P p-character and 9.3% P s-character), whereas the HOMO 1a$_2$ in PPh$_4^+$ is non-bonding aryl π^*. Despite the differences in symmetry and charge, the unoccupied MOs for both compounds have similar groups of MOs that can be classified according to their bonding between P and the phenyl groups. At lower energy are a cluster of MOs assigned to P-C bonding with phenyl π^* orbitals and MOs at higher energy are best described as P-C σ^*.

TDDFT was used to simulate the P K-edge XAS spectra of PPh$_3$ and PPh$_4^+$ using the ground-state DFT results provided in Fig. 6. The simulated spectra yield relatively good agreement with the experimental spectra once an energy shift was applied to account for errors in determining absolute energies, which is well established in ligand K-edge TDDFT calculations (Fig. 7) (Lee et al., 2016). For PPh$_3$, the first pre-edge feature was assigned to P 1s → 1e (P-C π^*) and the second feature at higher energy was assigned to P 1s → 3e (P-C σ^*). These both are formally assigned as ^{1}A→^{1}E, but we use the primary orbital contributions to the electronic states here and below to relate the transitions back to the MOs in Fig. 6. A higher-energy transition assigned to P 1s → 4a (P-C σ^*) was not observed in our data, presumably a result of masking by the OPPh$_3$ peak from photodecomposition. No transitions of significant intensity were calculated under the peak assigned to the OPPh$_3$ impurity at 2150.1 eV, consistent with its assignment to photodecomposition.

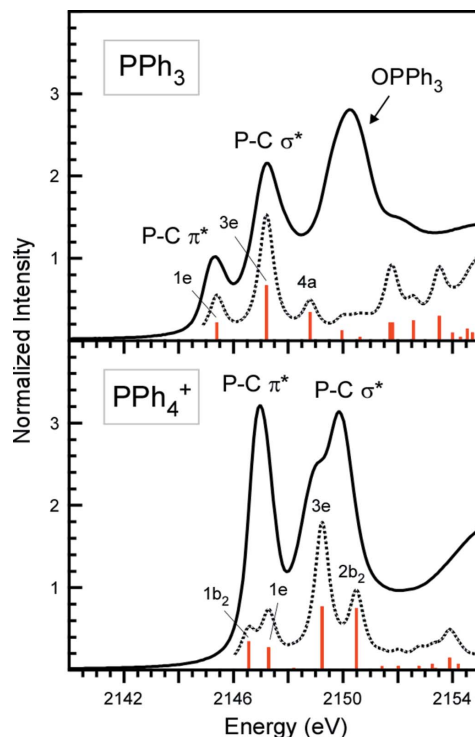The simulated spectrum for PPh$_4^+$ also provided relatively good agreement with its P K-edge XAS spectrum. The

Figure 7
Comparison of experimental (solid black line) and simulated (dashed black line) P K-edge XAS for PPh$_3$ (top; first scan from Fig. 2) and PPh$_4$Br (bottom) from TDDFT calculations. The transition energies and relative oscillator strengths are depicted as red bars. Major unoccupied orbital components contributing to the electronic transitions have been assigned to correspond to the Mulliken symbols from Fig. 6.

TDDFT spectrum indicates that the first feature at 2146.96 eV is attributed to a combination of two closely spaced transitions assigned to P $1s \rightarrow b_2$ and $1s \rightarrow e$ at 2146.55 and 2147.29 eV, respectively. The presence of two transitions in the TDDFT data accounts for the shoulder observed at ~2147.3 eV in the second derivative trace of the experimental spectrum (Fig. 4). Two P-C σ^* transitions calculated at 2149.24 and 2150.49 eV were assigned to P $1s \rightarrow 3e$ and $1s \rightarrow 2b_2$. These transitions account for the second and third features in the P K-edge spectrum. Overall, the TDDFT data corroborated the P K-edge results and allowed the features to be assigned to P $1s \rightarrow$ P-C π^* and $1s \rightarrow$ P-C σ^*. These findings are consistent with assignments previously made by Hormes based on MS Xα calculations for OPPh$_3$ and PPh$_3$ (Engemann *et al.*, 1999).

4. Conclusions

In summary, we presented the P K-edge XANES spectrum of PPh$_4$Br and compared it with other phosphorus compounds used as P K-edge energy calibration standards. In addition to its exceptional photostability and commercial availability, PPh$_4$Br has a highly resolved pre-edge feature at 2146.96 eV ideal for precise P K-edge XANES energy referencing. This peak was calibrated to the white line of Na$_4$P$_2$O$_7$ at 2152.40 eV (Küper *et al.*, 1994) and cross-referenced to the OPPh$_3$ pre-edge peak reported by Hormes and co-workers at 2147.3 eV (Engemann *et al.*, 1999). We have used PPh$_4$Br as a calibration standard for several P K-edge XANES data collection runs at SSRL (Lee *et al.*, 2016), and we saw no decomposition after repeated calibration scans on the same PPh$_4$Br sample during a week of P K-edge XANES data collection. DFT and TDDFT calculations were used to assign features in the P K-edge XANES spectrum of PPh$_4$Br, and the simulated spectrum from TDDFT corroborated our experimental results.

Overall, our analysis suggests that PPh$_4$Br is an excellent alternative to more commonly used energy calibration standards used for P K-edge XANES spectroscopy, especially for ligand K-edge XAS analysis of coordination complexes containing phosphorus ligands. As such, we propose that the PPh$_4$Br pre-edge position at 2146.96 eV be used for P K-edge energy calibration in future ligand K-edge XAS studies.

References

Adhikari, D., Mossin, S., Basuli, F., Huffman, J. C., Szilagyi, R. K., Meyer, K. & Mindiola, D. J. (2008). *J. Am. Chem. Soc.* **130**, 3676–3682.

Alcock, N. W., Pennington, M. & Willey, G. R. (1985). *Acta Cryst.* **C41**, 1549–1550.

Bauernschmitt, R. & Ahlrichs, R. (1996). *J. Chem. Phys.* **104**, 9047–9052.

Baumann, K., Glaser, K., Mutz, J.-E., Karsten, U., MacLennan, A., Hu, Y., Michalik, D., Kruse, J., Eckhardt, K.-U., Schall, P. & Leinweber, P. (2017). *Soil Biol. Biochem.* **109**, 156–166.

Becke, A. D. (1993). *J. Chem. Phys.* **98**, 5648–5652.

Blanchard, P. E. R., Grosvenor, A. P., Cavell, R. G. & Mar, A. (2008). *Chem. Mater.* **20**, 7081–7088.

Daly, S. R., Keith, J. M., Batista, E. R., Boland, K. S., Clark, D. L., Kozimor, S. A. & Martin, R. L. (2012). *J. Am. Chem. Soc.* **134**, 14408–14422.

Dey, A., Okamura, T., Ueyama, N., Hedman, B., Hodgson, K. O. & Solomon, E. I. (2005). *J. Am. Chem. Soc.* **127**, 12046–12053.

Donahue, C. M., Lezama Pacheco, J. S., Keith, J. M. & Daly, S. R. (2014). *Dalton Trans.* **43**, 9189–9201.

Donahue, C. M., McCollom, S. P., Forrest, C. M., Blake, A. V., Bellott, B. J., Keith, J. M. & Daly, S. R. (2015). *Inorg. Chem.* **54**, 5646–5659.

Dunne, B. J. & Orpen, A. G. (1991). *Acta Cryst.* **C47**, 345–347.

Engemann, C., Franke, R., Hormes, J., Lauterbach, C., Hartmann, E., Clade, J. & Jansen, M. (1999). *Chem. Phys.* **243**, 61–75.

Eveborn, D., Gustafsson, J. P., Hesterberg, D. & Hillier, S. (2009). *Environ. Sci. Technol.* **43**, 6515–6521.

Ferraz, M. P., Monteiro, F. J. & Manuel, C. M. (2004). *J. Appl. Biomater. Biomech.* **2**, 74–80.

Frisch, M. J. T. G. W., Schlegel, H. B., Scuseria, G. E., Robb, M. A., Cheeseman, J. R., Scalmani, G., Barone, V., Mennucci, B., Petersson, G. A., Nakatsuji, H., Caricato, M., Li, X., Hratchian, H. P., Izmaylov, A. F., Bloino, J., Zheng, G., Sonnenberg, J. L., Hada, M., Ehara, M., Toyota, K., Fukuda, R., Hasegawa, J., Ishida, M., Nakajima, T., Honda, Y., Kitao, O., Nakai, H., Vreven, T., Montgomery, J. A. Jr, Peralta, J. E., Ogliaro, F., Bearpark, M., Heyd, J. J., Brothers, E., Kudin, K. N., Staroverov, V. N., Kobayashi, R., Normand, J., Raghavachari, K., Rendell, A., Burant, J. C., Iyengar, S. S., Tomasi, J., Cossi, M., Rega, N., Millam, N. J., Klene, M., Knox, J. E., Cross, J. B., Bakken, V., Adamo, C., Jaramillo, J., Gomperts, R., Stratmann, R. E., Yazyev, O., Austin, A. J., Cammi, R., Pomelli, C., Ochterski, J. W., Martin, R. L., Morokuma, K., Zakrzewski, V. G., Voth, G. A., Salvador, P., Dannenberg, J. J., Dapprich, S., Daniels, A. D., Farkas, Ö., Foresman, J. B., Ortiz, J. V., Cioslowski, J. & Fox, D. J. (2009). *Gaussian 09*, Revision D.01. Gaussian Inc., Pittsburgh, Pennsylvania, USA.

Glaser, T., Hedman, B., Hodgson, K. O. & Solomon, E. I. (2000). *Acc. Chem. Res.* **33**, 859–868.

Grimme, S., Antony, J., Ehrlich, S. & Krieg, H. (2010). *J. Chem. Phys.* **132**, 154104.

Grosvenor, A. P., Cavell, R. G. & Mar, A. (2008). *J. Solid State Chem.* **181**, 2549–2558.

Hariharan, P. C. & Pople, J. A. (1973). *Theor. Chim. Acta*, **28**, 213–222.

Harkins, S. B., Mankad, N. P., Miller, A. J. M., Szilagyi, R. K. & Peters, J. C. (2008). *J. Am. Chem. Soc.* **130**, 3478–3485.

Hashimoto, Y., Takamoto, A., Kikkawa, R., Murakami, K. & Yamaguchi, N. (2014). *Environ. Sci. Technol.* **48**, 5486–5492.

Hehre, W. J., Ditchfield, R. & Pople, J. A. (1972). *J. Chem. Phys.* **56**, 2257–2261.

Hu, Y., Maclennan, A. & Sham, T. K. (2015). *J. Lumin.* **166**, 143–147.

Huang, R. & Tang, Y. (2016). *Water Res.* **100**, 439–447.

Ingall, E. D., Brandes, J. A., Diaz, J. M., de Jonge, M. D., Paterson, D., McNulty, I., Elliott, W. C. & Northrup, P. (2011). *J. Synchrotron Rad.* **18**, 189–197.

Kasrai, M., Vasiga, M., Suominen Fuller, M., Bancroft, G. M. & Fyfe, K. (1999). *J. Synchrotron Rad.* **6**, 719–721.

Kim, B., Gautier, M., Rivard, C., Sanglar, C., Michel, P. & Gourdon, R. (2015). *Environ. Sci. Technol.* **49**, 4903–4910.

Kozimor, S. A., Yang, P., Batista, E. R., Boland, K. S., Burns, C. J., Christensen, C. N., Clark, D. L., Conradson, S. D., Hay, P. J., Lezama, J. S., Martin, R. L., Schwarz, D. E., Wilkerson, M. P. & Wolfsberg, L. E. (2008). *Inorg. Chem.* **47**, 5365–5371.

Kozimor, S. A., Yang, P., Batista, E. R., Boland, K. S., Burns, C. J., Clark, D. L., Conradson, S. D., Martin, R. L., Wilkerson, M. P. & Wolfsberg, L. E. (2009). *J. Am. Chem. Soc.* **131**, 12125–12136.

Kraal, P., Bostick, B. C., Behrends, T., Reichart, G.-J. & Slomp, C. P. (2015). *Mar. Chem.* **168**, 1–8.

Kruse, J. & Leinweber, P. (2008). *J. Plant Nutr. Soil Sci.* **171**, 613–620.

Kruse, J., Negassa, W., Appathurai, N., Zuin, L. & Leinweber, P. (2010). *J. Environ. Qual.* **39**, 2179–2184.

Küper, G., Hormes, J. & Sommer, K. (1994). *Macromol. Chem. Phys.* **195**, 1741–1753.

Lee, C., Yang, W. & Parr, R. G. (1988). *Phys. Rev. B*, **37**, 785–789.

Lee, K., Wei, H., Blake, A. V., Donahue, C. M., Keith, J. M. & Daly, S. R. (2016). *Dalton Trans.* **45**, 9774–9785.

Liu, J., Hu, Y., Yang, J., Abdi, D. & Cade-Menun, B. J. (2015). *Environ. Sci. Technol.* **49**, 168–176.

Liu, J., Yang, J., Cade-Menun, B. J., Liang, X., Hu, Y., Liu, C. W., Zhao, Y., Li, L. & Shi, J. (2013). *J. Environ. Qual.* **42**, 1763–1770.

Löble, M. W., Keith, J. M., Altman, A. B., Stieber, S. C. E., Batista, E. R., Boland, K. S., Conradson, S. D., Clark, D. L., Lezama Pacheco, J., Kozimor, S. A., Martin, R. L., Minasian, S. G., Olson, A. C., Scott, B. L., Shuh, D. K., Tyliszczak, T., Wilkerson, M. P. & Zehnder, R. A. (2015). *J. Am. Chem. Soc.* **137**, 2506–2523.

Mankad, N. P., Antholine, W. E., Szilagyi, R. K. & Peters, J. C. (2009). *J. Am. Chem. Soc.* **131**, 3878–3880.

Minasian, S. G., Keith, J. M., Batista, E. R., Boland, K. S., Clark, D. L., Conradson, S. D., Kozimor, S. A., Martin, R. L., Schwarz, D. E., Shuh, D. K., Wagner, G. L., Wilkerson, M. P., Wolfsberg, L. E. & Yang, P. (2012). *J. Am. Chem. Soc.* **134**, 5586–5597.

Minasian, S. G., Keith, J. M., Batista, E. R., Boland, K. S., Clark, D. L., Kozimor, S. A., Martin, R. L., Shuh, D. K. & Tyliszczak, T. (2014). *Chem. Sci.* **5**, 351–359.

Morel, F. L., Pin, S., Huthwelker, T., Ranocchiari, M. & van Bokhoven, J. A. (2015). *Phys. Chem. Chem. Phys.* **17**, 3326–3331.

Mossin, S., Tran, B. L., Adhikari, D., Pink, M., Heinemann, F. W., Sutter, J., Szilagyi, R. K., Meyer, K. & Mindiola, D. J. (2012). *J. Am. Chem. Soc.* **134**, 13651–13661.

Nakahira, A., Nakata, K., Numako, C., Murata, H. & Matsunaga, K. (2011). *Mater. Sci. Appl.* **02**, 1194–1198.

Northrup, P., Leri, A. & Tappero, R. (2016). *Protein Pept. Lett.* **23**, 300–308.

Olson, A. C., Keith, J. M., Batista, E. R., Boland, K. S., Daly, S. R., Kozimor, S. A., MacInnes, M. M., Martin, R. L. & Scott, B. L. (2014). *Dalton Trans.* **43**, 17283–17295.

Oxmann, J. F. (2014). *Biogeosciences*, **11**, 2169–2183.

Pereira, G., Lachenwitzer, A., Munoz-Paniagua, D., Kasrai, M., Norton, P. R., Abrecht, M. & Gilbert, P. U. P. A. (2006). *Tribol. Lett.* **23**, 109–119.

Pereira, G., Munoz-Paniagua, D., Lachenwitzer, A., Kasrai, M., Norton, P. R., Capehart, T. W., Perry, T. A. & Cheng, Y.-T. (2007). *Wear*, **262**, 461–470.

Prietzel, J., Dümig, A., Wu, Y., Zhou, J. & Klysubun, W. (2013). *Geochim. Cosmochim. Acta*, **108**, 154–171.

Prietzel, J., Harrington, G., Häusler, W., Heister, K., Werner, F. & Klysubun, W. (2016). *J. Synchrotron Rad.* **23**, 532–544.

Queen, M. S., Towey, B. D., Murray, K. A., Veldkamp, B. S., Byker, H. J. & Szilagyi, R. K. (2013). *Coord. Chem. Rev.* **257**, 564–578.

Rafiuddin, M. R. & Grosvenor, A. P. (2016). *Inorg. Chem.* **55**, 9685–9695.

Rafiuddin, M. R., Mueller, E. & Grosvenor, A. P. (2014). *J. Phys. Chem. C*, **118**, 18000–18009.

Ravel, B. & Newville, M. (2005). *J. Synchrotron Rad.* **12**, 537–541.

Raynaud, S., Champion, E., Bernache-Assollant, D. & Thomas, P. (2002). *Biomaterials*, **23**, 1065–1072.

Sharma, V., Doerr, N. & Aswath, P. B. (2016). *RSC Adv.* **6**, 22341–22356.

Shearer, J., Callan, P. E., Masitas, C. A. & Grapperhaus, C. A. (2012). *Inorg. Chem.* **51**, 6032–6045.

Solomon, E. I., Hedman, B., Hodgson, K. O., Dey, A. & Szilagyi, R. K. (2005). *Coord. Chem. Rev.* **249**, 97–129.

Soma, S., Van Stappen, C., Kiss, M., Szilagyi, R. K., Lehnert, N. & Fujisawa, K. (2016). *J. Biol. Inorg. Chem.* **21**, 757–775.

Spencer, L. P., Yang, P., Minasian, S. G., Jilek, R. E., Batista, E. R., Boland, K. S., Boncella, J. M., Conradson, S. D., Clark, D. L., Hayton, T. W., Kozimor, S. A., Martin, R. L., MacInnes, M. M., Olson, A. C., Scott, B. L., Shuh, D. K. & Wilkerson, M. P. (2013). *J. Am. Chem. Soc.* **135**, 2279–2290.

Takamoto, A. & Hashimoto, Y. (2014). *Chem. Lett.* **43**, 1696–1697.

Tan, Y., Sun, D., Yu, H., Yang, B., Gong, Y., Yan, S., Chen, Z., Cai, Q. & Wu, Z. (2014). *CrystEngComm*, **16**, 9657–9668.

Yoshida, M., Mineo, T., Mitsutomi, Y., Yamamoto, F., Kurosu, H., Takakusagi, S., Asakura, K. & Kondoh, H. (2016). *Chem. Lett.* **45**, 277–279.

Zhang, Z., Yamaguchi, E. S., Kasrai, M. & Bancroft, G. M. (2005). *Tribol. Lett.* **19**, 211–220.